Typesetter Query for MAM2200051 AU Correction

1. As per Google search, we have inserted publisher location for below reference. Please check and confirm.

Witten IH, Frank E & Hall MA (2011). *Data Mining: Practical Machine Learning Tools and Techniques.* Amsterdam: Morgan Kaufmann, Elsevier.

2. We are not sure about the below comment. Please check and advise.

CM5 : Please add citation for Table 2, Table 3, Table 4. The city is ' Table 2-4 show the performance measures evaluated for the aorta, cardinal vein, and capillary, respectively.'

Original Article

A Machine Learning Method for Automated *In Vivo* Transparent Vessel Segmentation and Identification Based on Blood Flow Characteristics

Mingzhu Sun, Yiwen Wang , Zhenhua Fu, Lu Li, Yaowei Liu and Xin Zhao*

Institute of Robotics and Automatic Information System (IRAIS) and the Tianjin Key Laboratory of Intelligent Robotic (tjKLIR), Nankai University, Tianjin 300350, China

Abstract

In vivo transparent vessel segmentation is important to life science research. However, this task remains very challenging because of the fuzzy edges and the barely noticeable tubular characteristics of vessels under a light microscope. In this paper, we present a new machine learning method based on blood flow characteristics to segment the global vascular structure *in vivo*. Specifically, the videos of blood flow in transparent vessels are used as input. We use the machine learning classifier to classify the vessel pixels through the motion features extracted from moving red blood cells and achieve vessel segmentation based on a region-growing algorithm. Moreover, we utilize the moving characteristics of blood flow to distinguish between the types of vessels, including arteries, veins, and capillaries. In the experiments, we evaluate the performance of our method on videos of zebrafish embryos. The experimental results indicate the high accuracy of vessel segmentation, with an average accuracy of 97.98%, which is much more superior than other segmentation or motion-detection algorithms. Our method has good robustness when applied to input videos with various time resolutions, with a minimum of 3.125 fps.

Key words: blood flow, machine learning, microscopy images, region growing, vessel segmentation

(Received 10 December 2021; revised 10 March 2022; accepted 14 March 2022)

Introduction

Vasculature assessment plays a significant role in various fields of studies, including medical diagnoses (Francia et al., 2020), biomedical sciences (Yip et al., 2021), neuroscience (Li et al., 2017), and micromanipulation (Arcese et al., 2013). Among the various vasculatures, *in vivo* transparent vessels are a very special kind and are common in frogs and fish larvae, for example, see-through frogs, zebrafish embryos, and juvenile surgeonfish. *In vivo* transparent vessels can be observed directly using a light microscope, so researchers can observe the whole process of angiogenesis and evaluate the arteriolar-to-venular ratio (Daien et al., 2013; Seidelmann et al., 2016) to study vascular architecture, cardiovascular development, disease and the effect of drugs without complex preprocessing. Moreover, transparent vessels are used in some biological micromanipulations, such as *in vivo* cardinal vein microinjection (Sun et al., 2021), *in vivo* cell tracking (Menon et al., 2016), and blood flow velocity measurement (Chan & Liebling, 2015), since they provide a clear microscopic view to achieve real-time visual feedback.

It is important to obtain the blood vessel region, especially the region of *in vivo* transparent vessels. Automated segmentation of the vasculature provides crucial information, such as vessel diameters, length, branching patterns and tortuosity, for quantitative analysis and visualization, which greatly reduces the difficulty and improves the efficiency of subsequent research. According to the source of the vessels, vessel segmentation can be divided into human vessel segmentation and animal vessel segmentation.

For humans, vessel imaging depends on the location of vessels in the body. For example, laparoscopic ultrasound (LUS) is used to visualize subsurface structures, including liver vessels, magnetic resonance angiography (MRI) is applied to visualize brain vessels, computed tomography (CT) aids in pulmonary vessel and renal artery visualization, and a fundus camera captures retinal images. Therefore, researchers have proposed a variety of vessel segmentation methods for different types of vessels. Yan et al. (2020) proposed an attention-guided deep neural network with multiscale feature fusion for liver vessel segmentation. Phellan et al. (2018) used the ranking orientation responses of path operators and multiscale vesselness enhancement filters to enhance brain vessels and performed segmentation using a seed-based algorithm. Wang et al. (2019) modeled each voxel by a second-order tensor to capture the intensity information and the geometric information for renal artery segmentation. Xu et al. (2018) proposed the stage-wise convolutional networks followed by an orientation-based region-growing method for pulmonary vessel segmentation. Unlike the above vascular images, retinal images are usually color images. Retinal vessel segmentation methods in recent years include a dedicated end-to-end matting algorithm to retrieve vessel pixels in thin and tiny vessels (Zhao et al., 2019), a split-based coarse-to-fine vessel segmentation network to detect

thick and thin vessels separately (Ma et al., 2021), a combination of a Hessian-based approach and an intensity transformation approach to segment retinal fundus images in an unsupervised way (Alhussein et al., 2020), and a recursive semantics-guided U-shaped network to improve the connectivity of segmented vessels (Xu et al., 2020). These methods exhibit great performance in human vessel segmentation. However, human vessel images are quite different from microscopic images of transparent vessels. These methods are not suitable for transparent vessel segmentation.

Animal vessel segmentation is usually used in disease and drug research. Animals, such as zebrafish and mice, are genetically modified or infected by viruses so that fluorescent vascular images can be taken by two/multiphoton microscopy or confocal microscopy. To date, many efforts have been devoted to segmenting fluorescence microscopic images of certain animal vessels. The open-source software Fiji was applied to segment transgenic fluorescent vasculature images (Schindelin et al., 2012; Kugler et al., 2019). A dual ResUNet model was proposed to detect more information for overlapping regions caused by an uneven distribution of fluorescence intensities (Zhang et al., 2019). Ip et al. (2002) described an automated technique for segmenting, tracking, and identifying the tail vessels of zebrafish embryos using serial fluorescent images. A framework was introduced in Feng et al. (2005) for automatic segmentation and registration of different kinds of blood vessels. Yang & Xu (2017) studied the recognition of zebrafish interstitial blood vessels based on Haar-like features and an improved AdaBoost network model. Fluorescence microscopic imaging has high contrast and a low signal-to-noise ratio (SNR), but the process of fluorescence image acquisition is complex and time-consuming. Moreover, the experimental animals usually die after long-term fluorescence observation due to the high intensity of lasers, which may affect follow-up research.

For transparent animals and embryos, such as zebrafish embryos, it is more convenient to directly observe blood vessels and blood flow through light microscopy. However, it is difficult to segment transparent vessels by using a single microscopic image. As shown in Figure 1a, the vascular boundaries cannot be defined precisely due to the fuzzy edges and the barely noticeable tubular characteristics. Therefore, a simple and automatic segmentation method for *in vivo* transparent vessels can effectively improve the efficiency of relevant research.

To the best of our knowledge, there have been few works on *in vivo* transparent vessel segmentation to date. We discovered that red blood cells (RBCs) in vessels are obvious when they are moving, and their motion trajectory indirectly represents the vascular shape. Inspired by this, we present an *in vivo* transparent vessel segmentation and identification method based on blood flow characteristics, which only requires a short video of blood flow under a light microscope. The basic idea of the proposed method is to identify the transparent vessel pixels by the moving RBCs using a special set of motion features and the adaptive nature of machine learning. Specifically, the motion features are extracted from the moving RBCs and used to train a machine learning classification model. Then, the vascular structure is generated based on a region-growing algorithm, in which each vessel pixel is classified iteratively using a machine learning classifier. Furthermore, the moving characteristics of the blood flow are utilized to distinguish between the types of vessels, that is, arteries, veins, and capillaries. In the experiments, the segmentation result of the global vascular structure is obtained with an average accuracy of 97.98% for the specific application to zebrafish embryos.

The major contributions of the proposed method are summarized as follows:

1) We achieve indirect *in vivo* transparent vessel segmentation by analyzing the motion of RBCs in vessels. We only use short videos of blood flow under a light microscope as the input of segmentation and do not need to visualize the vessels laboriously by confocal microscopy, which makes the method more practicable and user friendly than traditional fluorescent segmentation methods. This is the first work that approaches the difficulty of transparent vessel segmentation from this perspective.

2) We design two flow-connectivity features coupled with two vessel-connectivity features and several grey-level statistical features for classification, inspired by the continuity of RBC motion in the neighboring frames. The flow-connectivity features provide motion distribution information on the RBCs, which helps detect the motion of the slow-moving cells to further identify the thin vessel pixels and suppress the background noise.

3) We classify the vessels as arteries, veins, or capillaries according to the direction and magnitude of the velocity vectors in the vessel regions. Due to the continuous motion, the change in the direction and magnitude of the velocity vectors is continuous in one vessel but discrepant in different vessels, enabling the separation of different blood vessels and further distinguishing between their types. This work may assist in research on specific vessels.

Materials and Methods

The main idea of the proposed method is to identify the vessel pixels by observing moving RBCs using a special set of motion features and the adaptive nature of machine learning. The method
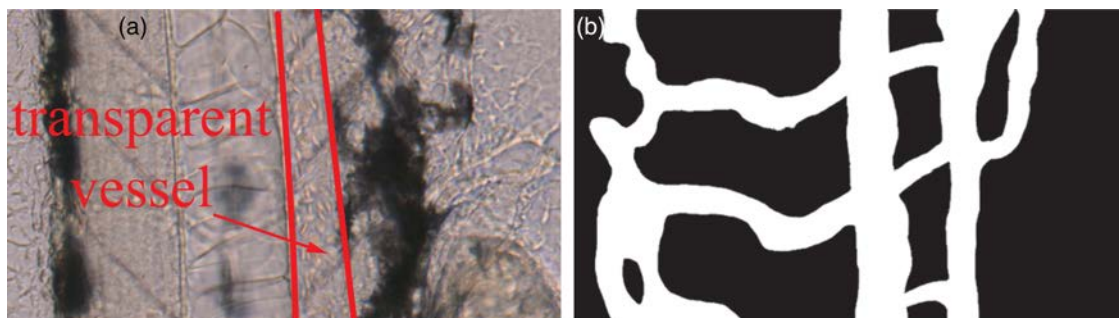
Fig. 1. Example of transparent vessels. (**a**) Light microscope image of a part of zebrafish embryo vessels. (**b**) Ground truth of the corresponding vessel segment of (**a**).

consists of three main steps: (1) optical flow calculation and motion feature extraction, (2) vessel segmentation by region growing coupled with machine learning-driven pixel classification, and (3) vascular-type identification based on the motion information.

Figure 2 shows the workflow of the proposed method. In the first step, we calculate the dense optical flow of the moving RBCs and then extract the motion features. The machine learning classifier is trained and stored based on the features of the ground truth. In the second step, the seed points of the region-growing algorithm are selected automatically using two basic segmentation methods. Then, we use machine learning classifiers to classify each candidate pixel as a vessel or nonvessel pixel and conduct region growing for vessel segmentation. In the last step, we identify the vessels according to the moving characteristics of the

blood flow and the position of the heart of the animals. In Figure 2, the red arrows between the dashed boxes represent the motion feature updated after each iteration in region growing. The blue arrows show the data flow of the average optical flow field, which will be reused further in seed point selection and vascular-type identification. The green arrow indicates that the segmentation results of the vascular structure are utilized as the constraint for vascular-type identification.

Motion Feature Extraction

In the videos of blood flow, RBCs move fast and obviously in the main vessels, while they move slowly and weakly in the capillaries due to the vessel diameter and the number of circulating RBCs.
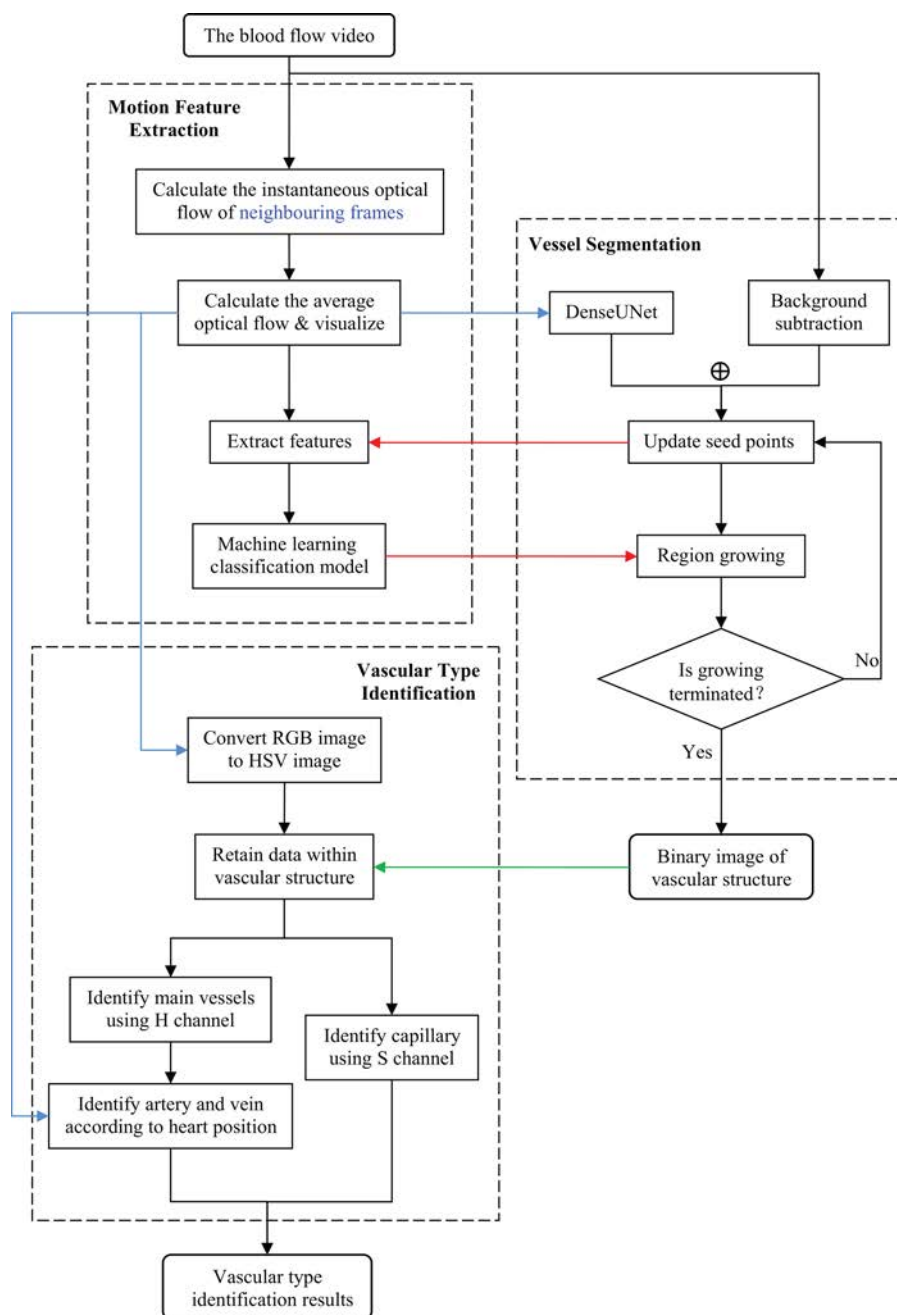

Fig. 2. Flowchart of the proposed method.

Thus, capillary segmentation is much more difficult than main vessel segmentation. Motion has the property of continuity and regularity in the interframe of the video, that is, there is a higher probability that the pixels, which are neighbors of the moved pixels, belong to the moving object. Therefore, motion connectivity can assist in detecting the moved pixels, especially the pixels with slow motion. In this paper, we calculate the instantaneous optical flow field of every two consecutive frames in the video using the dense optical flow algorithm *Farneback* (Farnebck, 2003) to obtain motion velocity vectors of all pixels and calculate the average optical flow field for background noise suppression. This average dense optical flow field contains the total motion information of the video. Based on the optical flow field, we design the flow-connectivity features to identify the moved pixels, that is, the vessel pixels.

In region-growing-based segmentation algorithms, connectivity is a central principle. However, region growing alone cannot produce sufficiently accurate segmentation results. In this paper, we use redesigned region growing coupled with machine learning-driven pixel classification (Rodrigues et al., 2020) to improve the adaptivity. The pixels belonging to vascular structures are updated in time as the per-pixel classification process advances. Classification occurs in a region-growing fashion, which also improves the efficiency and accuracy. In addition, Rodrigues et al. (2020) indicated the good performance of vessel-connectivity features combined with grey-level pattern information in classification. Hence, we modify these features and classify the vessel pixels along with the flow-connectivity features.

Three kinds of features, the flow-connectivity features, vessel-connectivity features, and grey-level features, are combined to provide an information-rich vector for pixel classification. The flow-connectivity features provide information that defines whether a pixel is near another moving pixel using the average optical flow field. The vessel-connectivity features help detect the possible vessel pixels in the neighborhood of the vessels using the binary image of the vascular structure. The grey-level features assist in identifying border pixels using the visualized image of the average optical flow field. We provide details of flow-connectivity features and briefly introduce the information of vessel-connectivity features and grey-level statistical features as follows.

1) *Flow-connectivity Features* (Two Features): Two flow-connectivity features are extracted from the average optical flow field of the input video, including an immediate flow-connectivity feature and a radial flow-connectivity feature. The immediate flow-connectivity feature focuses on the 8 neighbors of the current candidate pixel and uses a probability function to determine the number of pixels whose velocity vectors are similar to the motion vectors. The immediate flow-connectivity feature of the current candidate pixel $I_{i,j}$ is defined as

$$f_i(I_{i,j}) = \begin{cases} 1, & \text{if } P_i(I_{i,j}) > T_i, \\ 0, & \text{otherwise,} \end{cases} \quad (1)$$

where T_i is the threshold for selecting the candidate motion vector in the 8 neighbors with high probability $P_i(I_{i,j})$. $P_i(I_{i,j})$ is given by

$$P_i(I_{i,j}) = \frac{e^{M_{i,j}} - 1}{Norm_i}, \quad (2)$$

where $Norm_i$ is a normalizing constant used to ensure that the probability does not exceed 1, and

$$M_{i,j} = \sum_{m,n \in k} (isSimilar(v_{i,j}, v_{i+m,j+n}) \cap isVessel(I_{i+m,j+n})), \quad (3)$$

where k denotes the 8 neighbors of the current candidate pixel $I_{i,j}$, $isSimilar(v_{i,j}, v_{i+m,j+n})$ determines whether two velocity vectors are similar, and $isVessel(I_{i+m,j+n})$ determines whether pixel $I_{i+m,j+n}$ belongs to the vessel, that is, whether the velocity vector of $I_{i+m,j+n}$ is a motion vector. They are calculated as follows:

$$isSimilar(v_1, v_2) = \begin{cases} 1, & \text{if } (\cos(v_1, v_2) > T_{\cos}) \\ & \cap (||v_1| - |v_2|| < T_{\text{speed}} \cdot |v_2|), \\ 0, & \text{otherwise,} \end{cases} \quad (4)$$

$$isVessel(I_{i,j}) = \begin{cases} 1, & \text{if } I_{i,j} == 255, \\ 0, & \text{otherwise,} \end{cases} \quad (5)$$

where $T_{\cos}$ is the angle threshold and T_{speed} is the magnitude ratio threshold of two vectors.

The radial flow-connectivity feature focuses on a circular neighborhood of the current candidate pixel, which aims to consider disconnected moving cells. The radial flow-connectivity feature of the current candidate pixel $I_{i,j}$ is defined as follows:

$$f_r(I_{i,j}) = \begin{cases} 1, & \text{if } P_r(I_{i,j}) > T_r, \\ 0, & \text{otherwise,} \end{cases} \quad (6)$$

where T_r is the threshold used to select the candidate motion vector in the circular neighbors with a high probability $P_r(I_{i,j})$. As defined in equation (7), $P_r(I_{i,j})$ uses the logarithmic function instead of the exponential function in equation (2) to calculate the similarity because a broader sliding region and more candidate pixels easily cause the overflow of the results achieved by the exponential function. Similarly, $Norm_r$ is also a normalizing constant used to ensure that the probability does not exceed 1, and $M_{i,j}$ is calculated by the same formula, that is, equation (3), of which k denotes the circular neighbors of $I_{i,j}$.

$$P_r(I_{i,j}) = \frac{\ln(M_{i,j} + 1)}{Norm_r}. \quad (7)$$

2) *Vessel-connectivity Features* (Two Features): Two vessel-connectivity features are extracted from the seed point image processed during region growing. Similar to the flow-connectivity features, vessel-connectivity features include an immediate vessel-connectivity feature and a radial vessel-connectivity feature, which consider 8 neighbors and the circular neighborhood of the current candidate pixel. The immediate vessel-connectivity feature is defined as

$$v_i(I_{i,j}) = \begin{cases} 1, & \text{if } P_i(I_{i,j}) > T_i, \\ 0, & \text{otherwise,} \end{cases} \quad (8)$$

where $P_i(I_{i,j})$ is calculated by equation (2), of which $M_{i,j}$ is redefined as

$$M_{i,j} = \sum_{m,n \in k} isVessel(I_{i+m,j+n}). \quad (9)$$

The radial vessel-connectivity feature is defined as

$$v_r(I_{i,j}) = \begin{cases} 1, & \text{if } P_r(I_{i,j}) > T_r, \\ 0, & \text{otherwise}, \end{cases} \quad (10)$$

where $P_r(I_{i,j})$ is calculated by equation (7), of which $M_{i,j}$ is given by equation (9).

3) *Grey-level Statistical Features* (53 Features): Given the visualized image of the average optical flow field, the grey-level features are obtained from various image processing techniques including the (1) the difference of Gaussians filter (Cho et al., 2007) (four features), (2) the Hessian matrix (Lorenz et al., 1997) (ten features), (3) the Frangi filter (Frangi et al., 1998) (three features), (4) the Laplacian filter (İlk et al., 2011) (three features), (5) intensity statistics, including mean, max, min, and median values (five features), (6) anisotropic diffusion (Perona & Malik, 1990) (two features), (7) morphological opening and closing (Vincent, 1994) (six features), (8) image gradients (three features), (9) the Kuwahara filter (Bartyzel, 2016) (two features), (10) the Gabor filter (Kim et al., 2018) (four features), (11) high-order derivatives (Oszust, 2018) (four features), (12) entropy (Rajalaxmi & Nirmala, 2014) (three features), (13) the Sobel filter (Yaacoub & Daou, 2019) (two features), (14) the shake effect (Flusser et al., 2016) (one feature), and (15) the enhancement filter (Dong et al., 2008) (one feature). As most of these features are well known, we refer readers to the references within.

Prior to segmentation, the machine learning classifier is trained to generate a predictive model using the motion feature vectors extracted from the videos with the ground truth, including manually annotated binary images (i.e., each pixel belongs or does not belong to a vessel), the average optical flow field and visualized images. The classifier learns to associate specific feature patterns with labels during training and uses this information to produce a label when it is unknown, that is, in the testing phase. Because of the good adaptation to the specifics of the datasets, a random forest (Witten et al., 2011) is chosen as the machine learning classifier to conduct the experiments.

Vessel Segmentation

We use the extracted motion features to conduct vessel segmentation. As previously described, we classify the candidate pixels using the per-pixel machine learning classifier in a region-growing fashion. Each pixel is classified as either a vessel pixel or nonvessel pixel, where all the classification results form a binary image, representing the final segmentation of the vascular structure.

Initially, we obtain the seed points of region growing in three steps. First, the visualized image of the average optical flow field is segmented using DenseUNet (Li et al., 2018; Cai et al., 2020; Guan et al., 2020), a widely used image segmentation network with high precision, to achieve a preliminary binary result I_D. The binary image I_D has good connectivity. However, the large differences in vessel diameters and the numbers of moving RBCs between the main vessels and the narrow vessels make the motion velocities significantly different in vessels of different sizes. Due to the limitation of visualization techniques, the visualized image may only provide information about the main vessels

and ignore capillaries. Hence, the binary image I_D lacks precision, especially in capillaries. We apply background subtraction based on the Gaussian mixture model (Zivkovic & Heijden, 2006) to the input video as the second step to accumulate the transient motion change. We achieve another preliminary binary result I_B, which contains part of the capillary structure. Although I_B lacks continuity, it provides more detailed basic information of the narrow vessels. Last, after removing some slightly connected components, binary images I_D and I_B are added to obtain the seed point image I_S, where the pixels in the connected components are selected as the seed points.

Given the selected seed points, we extract the entire vascular structure through a region-growing method. S is the position set of the vessel pixels, that is, seed points. The unknown pixels in the 8 neighbors of the pixels in S are chosen as the candidate pixels for classification.

The detailed information of set S_i in the ith ($i \geq 1$) iteration is described as

$$S_0 = \{(x, y)|(x, y) \in I_S\}, \quad (11)$$

$$S_i = S_{i-1} \cup \{(x, y) \mid Classifier(v(x, y)) == 1, \\ ||S_{i-1}, (x, y)|| \leq \sqrt{2}\}, \quad (12)$$

where S_0 contains the initially selected seed points from seed point image I_S. At the ith iteration, each candidate pixel is chosen from the 8 neighbors of vessel pixels in set S_{i-1}. The motion feature vector $v(x,y)$ of the candidate pixel is extracted based on the previous classification information in its vicinity and is fed into the machine learning classifier to decide whether this pixel is a vessel pixel. If the classification result of pixel(x,y), $Classifier(v(x,y))$, is equal to 1, it will be added into set S_i.

Set S is updated after each iteration in region growing, which makes the flow-connectivity features and the vessel-connectivity features update in time as well. This means that if the candidate pixel is classified as a vessel pixel, the vessel pixel contribution in the neighborhood will be updated and then affect the evaluation of the connectivity features in the next iteration of motion feature extraction. This updated pixel information can significantly benefit subsequent pixel classification in the vicinity.

The classification process starts at iteration 0 from set S_0 containing the initially selected seed points and is terminated when all the pixels in the image are classified in the previous iteration. Finally, the segmented result, I_R, is obtained. The implemented pseudocode is described in Algorithm 1.

Algorithm 1. Vessel Segmentation
Inputs: The blood flow video *V*
1:
for each two frames in *V* **do**
2:
$F_{instant} \leftarrow$ calculate the instantaneous optical flow field using the *Farneback* algorithm
3:
ArrayList $\leftarrow$ *ArrayList* $\cup F_{instant}$
4:
end for

5:
$F_{avg} \leftarrow$ calculate the average optical flow field using *ArrayList*
6:
$I_{avg} \leftarrow$ visualize F_{avg} using the Munsell color system
7:
$I_D \leftarrow$ segment I_{avg} using DenseUNet
8:
$I_B \leftarrow$ accumulate the background subtraction results of V
9:
$I_S \leftarrow I_D \cup I_B$
10:
$S_0 \leftarrow I_S$
11:
Initialize the motion features of all pixels using F_{avg}, I_{avg}, and S_0
12:
Repeat
13:
$S_i \leftarrow S_{i-1} \cup \{(x, y) \mid Classifier(v(x, y)) == 1, \|S_{i-1}, (x, y)\| \leq \sqrt{2}\}$
14:
Update the motion features of each pixel using F_{avg} and S_i
15:
Until all pixels in I_s are classified
16:
$I_R \leftarrow S > 0$
Output: The segmented vessel image I_R

Vascular-Type Identification

After vessel segmentation, we distinguished the types of vessels from the entire vascular structure of the animals. Motion has the property of continuity and regularity in time. Notably, motion is usually continuous in the inner moving object but varies between different objects. This means that the velocity of moving cells changes continuously in the same vessel and varies considerably in different vessels. This motivates us to identify different types of vessels, including arteries, veins, and capillaries, based on the average optical flow field, which contains the motion information of the RBCs in all the vessels.

Inspired by the principle of manual identification, we use the location of the heart of animals as a reference to distinguish between arteries and veins. It is easy to recognize the heart in blood flow videos because of its powerful beating. The heart is the endpoint of the main vascular structure. Once the heart is located, the arteries and veins in the videos can be identified. The method of vascular-type identification is as follows. Taking the zebrafish embryo as an example, Figure 3 shows the workflow.

First, the visualized image of the average optical flow field is converted to the linear HSV color space from the nonlinear RGB color space (Fig. 3c), as shown in Figure 3d. The only data within the vascular structure are retained according to the vessel segmentation results, as shown in Figure 3e. By limiting the calculation range, we reduce the interference of the nonvascular region and improve the speed and accuracy of recognition. The
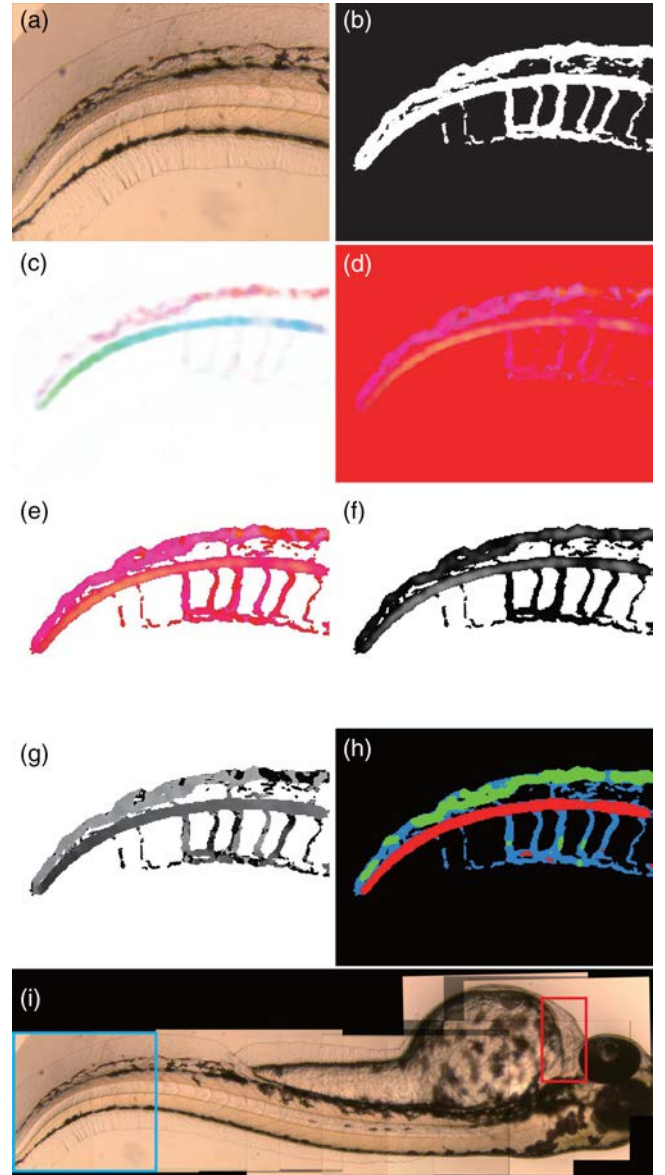

Fig. 3. Workflow of the proposed vascular-type identification method applied to the zebrafish embryo. (**a**) Local image of a zebrafish embryo under a light microscope; (**b**) vascular structure of (**a**); (**c–d**) visualized image of the average optical flow field of (**a**) in RGB color space and HSV color space, respectively; (**e**) HSV image of (**d**) within the vascular structure; (**f**) visualized image of the S channel of (**e**); (**g**) visualized image of the H channel of (**e**); (**h**) vascular-type identification result (red: artery; green: vein; and blue: capillary); and (**i**) global stitching image of the zebrafish embryo under a light microscope (the red bounding box represents the position of the heart, and the blue bounding box represents the local region of (**a**)).

continuous change in the colors in the HSV color space indirectly indicates the movement of the RBCs with continuous changes in velocity, which helps identify individual vessels.

Second, we extract the S channel of the HSV image, as shown in Figure 3f, and calculate its histogram of saturation. It is obvious that the speed of the blood cells in the capillaries is much lower than that in the main vessels. Hence, the saturation of the capillary area is clearly lower than that of the main vessels in the visualized image. We take the minimum saturation value between the peaks of the histogram as the threshold and mark the pixels with saturation values below the threshold as capillary pixels, so the capillaries are identified first.

Third, we extract the H channel of the HSV image, as shown in Figure 3g, to calculate a histogram of its hue values and take the two minimum values between the three peaks as double thresholds, α and β ($0 < \alpha < \beta < 180$). Because arterial blood flows from the heart and venous blood flows into the heart, the RBCs in the two main vessels flow in opposite directions, which makes the visualized vessels display marked differences in color between the two main vessels. Hence, the distribution of hue values helps distinguish between the two main vessels. The pixels with hue values between α and β are denoted pixels belonging to one main vessel, and the remaining pixels belong to the other main vessel.

Finally, the aorta and cardinal vein are identified from two main vessels by calculating the angle γ between the optical flow vector in the main vessel and the position of the heart. The main vessel with vectors pointing toward the heart ($\gamma < 90°$) is the cardinal vein, and the other vessel is the aorta. Figure 3i shows the global stitching image of the zebrafish embryo under a light microscope, where the red bounding box represents the position of the heart and the blue bounding box represents the local region to be processed, as shown in Figure 3a. The heart is located on the upper right of the target region. Figure 3h shows the final vascular-type identification result, where the red and green vessels represent the aorta and cardinal vein, respectively, and the blue vessels represent the capillaries.

Results

Zebrafish embryos are a widely used vertebrate model organism with transparent vessels and high fecundity. In this paper, we observed the blood flow of zebrafish embryos and conducted quantitative and qualitative transparent vessel segmentation and identification experiments.

Sample Preparation and Video Acquisition

We conducted the experiments with the embryos 60 h postfertilization (hpf), which were cultured in PTU medium with less melanin and cleaner fields. The zebrafish embryos were prepared according to protocols and procedures approved by the Animal Experimental Committee of Nankai University (No. 2008) and were operated on in accordance with the NIH Guide for the Care and Use of Laboratory Animals.

The videos of zebrafish embryo blood flow were acquired by a micromanipulation system, as shown in Figure 4. We used a motorized inverted microscope (TiE, Nikon) with a 10× objective (NA: 0.25) for observation. The zebrafish embryo was laid on its side in a Petri dish and carried into the field of view of the microscope by a motorized X-Y stage (ProScan III, Prior) with a motion range of 120 mm × 80 mm and a positioning resolution of 0.05 μm. A high-speed camera (PHANTOM, MIRO C110) was mounted on the microscope to capture videos of blood flow.

We first moved the motorized stage until the head of the embryo appeared in the field of view and focused on the RBCs in the vessels. Then, we captured a video of the blood flow in the current field of view for approximately 2 s by a high-speed camera at 50 fps. We moved the motorized stage in the direction from the head to the tail of the embryo and captured the video in each part of the embryo. Then, a long video was created and saved locally. We cut short videos from the whole original video for convenience. The short videos show the blood flow of different parts of the zebrafish embryo, constituting a complete vascular image.
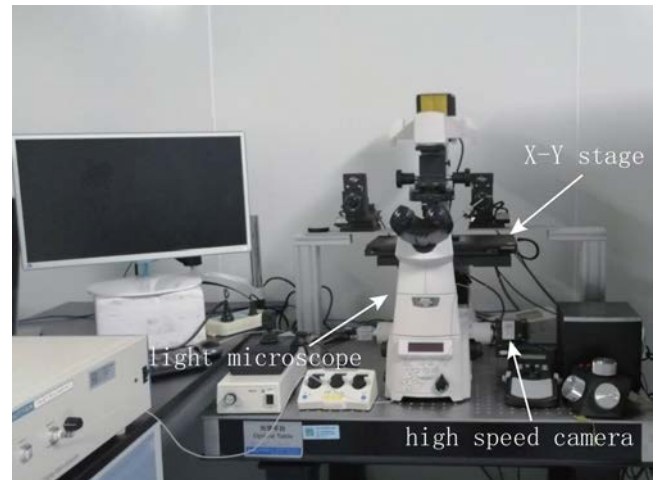

Fig. 4. Micromanipulation system setup.

We took a total of four complete videos on the blood flow of the zebrafish embryos. Seven to nine short videos were obtained for the local vessel parts of each zebrafish embryo after clipping.

Training of the Machine Learning Classifier and DenseUNet

There is currently no public database for zebrafish embryo blood vessels, so we used the binary images segmented manually by experienced biologists from the videos of blood flow as the ground truth. In the binary images, all the vessel pixels were classified into one of three classes: the aorta, cardinal vein, and capillary. The average optical flow field of the corresponding video was calculated using the *Farneback* optical flow algorithm and visualized by the Munsell color system.

For random forest classifier training, the classifier was trained using a ground truth binary image, the average optical flow field, and its visualized image of the video of zebrafish embryo blood flow. A single set of training data had approximately 164,000 feature vectors and was deemed sufficient for training, as there was not much variation among different videos.

DenseUNet was implemented for optical flow field image segmentation using the Keras open-source deep learning library. Because the visualized image of the average optical flow field directly showed the typical vascular branching structure, such as retinal vessel images, and did not involve the unique characteristics of the individual animals, we trained DenseUNet by using the retinal fundus image benchmark DRIVE (Staal et al., 2004). DRIVE consisted of 40 retinal images, where 20 images were marked as the training set and testing set. We trained DenseUNet with RMSprop, with an initial learning rate of 10^{-3} and an exponential decay of 0.995 after each epoch. The network was initialized using the Xavier method.

Training and deployment of DenseUNet were conducted on a PC equipped with an Intel i7 CPU with 512 GB of main memory and an NVIDIA GeForce GTX 1080Ti GPU. The other parts of the proposed method, including the random forest classifier, were implemented in C++ on a desktop PC with an Intel(R) Core (TM) i7-8700 CPU and 16.0 GB of RAM. The source code can be found in the supplementary material.

Evaluation Metric

To evaluate the performance of the proposed method, seven evaluation metrics were calculated, including accuracy (ACC),

precision, recall, harmonic mean F-measure (F_1), Jaccard similarity (JS), Matthews correlation coefficient (MCC), and area under the receiver operating characteristic (ROC) curve (AUC). The ACC is used to measure the proportion of correct predictions. Precision means that the true positive sample accounts for the proportion of all positive samples, and recall measures the proportion of positives that are correctly identified, while F_1 is used to balance precision and recall. The MCC is a measure of the quality of a binary classification and is suitable for vessel images with imbalanced amounts of foreground and background pixels. The JS evaluates the similarity between the ground truth and the segmentation result. The AUC is used to measure the performance of a binary segmentation method. These metrics are defined as follows:

$$\text{ACC} = \frac{\text{TP} + \text{TN}}{\text{TP} + \text{TN} + \text{FP} + \text{FN}}, \tag{13}$$

$$\text{Precision} = \frac{\text{TP}}{\text{TP} + \text{FP}}, \tag{14}$$

$$\text{Recall} = \frac{\text{TP}}{\text{TP} + \text{FN}}, \tag{15}$$

$$F_1 = 2 \times \frac{\text{Precision} \times \text{Recall}}{\text{Precision} + \text{Recall}}, \tag{16}$$

$$\text{JS} = \frac{|\text{GT} \cap \text{SR}|}{|\text{GT} \cup \text{SR}|}, \tag{17}$$

$$\text{MCC} = \frac{\text{TP} \times \text{TN} - \text{FP} \times \text{FN}}{\sqrt{(\text{TP} + \text{FP})(\text{TP} + \text{FN})(\text{TN} + \text{FP})(\text{TN} + \text{FN})}}, \tag{18}$$

where TP is the number of correctly segmented foreground pixels, TN represents the number of correctly segmented background pixels, FP is the number of incorrectly segmented foreground pixels, FN is the number of true foreground pixels that are not segmented as such, GT is the ground truth, and SR is the segmentation result.

Segmentation Results

We examined the segmentation performance of our method on the full image level to evaluate the overall performance in both the main vessels and the narrow vessels. For each zebrafish embryo, we reused the proposed method on each short video of blood flow and stitched all the segmentation results into one global image based on SIFT to obtain the global vascular structure.

Table 1 shows the quantitative performance of the proposed method on four zebrafish embryos. The average accuracy of all four zebrafish embryo vessel structures is 0.9798. Meanwhile, the method achieves both a high F_1 value of 0.8365 and a recall rate of 0.8308 on average. The average MCC is more than 0.82, and the average JS is 0.72. This means that the vessel structure in the segmented images produced by our method may be very close to the ground truth.

Figure 5 shows the qualitative global segmentation results. The magnified views are displayed beside the segmentation results in Figures 5b and 5c for more local details. Compared with the ground truth, the key structures of the aorta and cardinal vein of the zebrafish embryos are fully segmented, as well as most parts of the capillary structures. The segmentation results have good continuity and integrity and show the obvious branching feature of vessels.

Validation of Vascular Types

According to the segmentation results of the zebrafish embryos, we experimented with the proposed vascular-type identification method and performed classification validation on three types of vessels, that is, the aorta, cardinal vein, and capillary, from both quantitative and qualitative perspectives.

Tables 2–4 show the performance measures evaluated for the aorta, cardinal vein, and capillary, respectively. The average accuracy of the aorta and cardinal vein is both more than 0.98. Meanwhile, the capillary has an average accuracy of 0.9697. However, the average recall values of the cardinal vein and capillary are 0.3349 and 0.4311, respectively. These evaluation data indicate that the classification results have high accuracy in identifying the aorta but, to a certain extent, misclassify the cardinal vein and capillary.

Figure 6 depicts the global vascular-type identification results of four zebrafish embryos, where red and green vessels represent the aorta and cardinal vein, respectively, and blue vessels represent the capillaries. Compared with the ground truth, most of the red aortas are classified accurately, as are the blue capillaries. In addition, the proposed method classifies the green cardinal vein in the tail. The overall visual results display the passable continuity and integrity of the three vascular types.

Segmentation Comparison and Analysis

Further validation of the proposed method was completed by comparing with seven segmentation algorithms, ViBe (Barnich & Droogenbroeck, 2011), KNN (Jodoin & Mignotte, 2005),

Table 1. Quantitative Results of the Proposed Method on Each Zebrafish Embryo.

No	ACC	Precision	Recall	F_1	JS	MCC
1	0.9826	0.9281	0.8622	0.8939	0.8082	0.8852
2	0.9755	0.8639	0.7447	0.7998	0.6664	0.7894
3	0.9757	0.7282	0.8469	0.7831	0.6435	0.7728
4	0.9855	0.8692	0.8693	0.8693	0.7688	0.8616
Average	0.9798	0.8474	0.8308	0.8365	0.7217	0.8273

(a) Zebrafish embryo images   (b) Ground truth   (c) Segmentation results
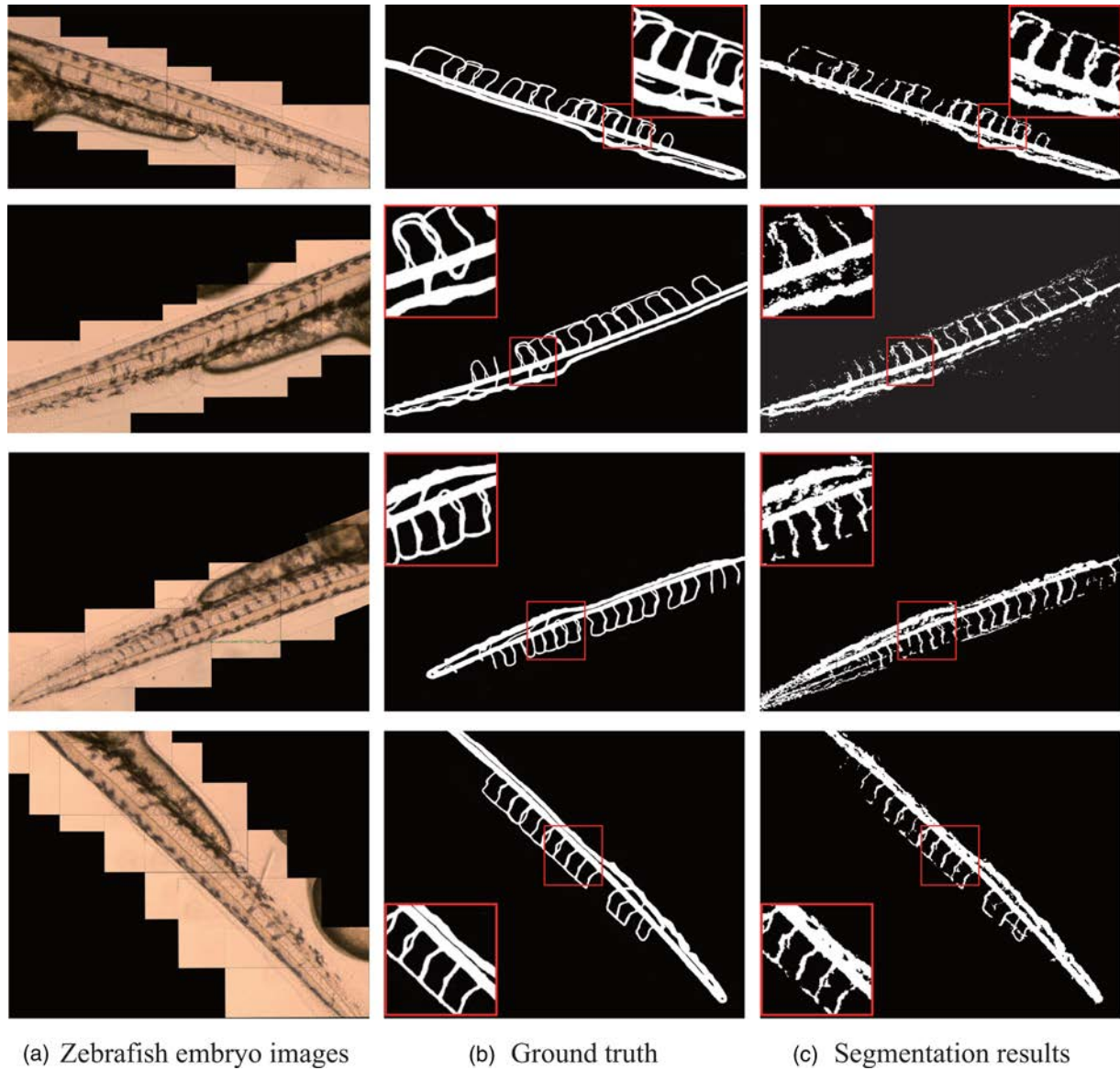
Fig. 5. Global segmentation results of four zebrafish embryos.

Table 2. Quantitative Classification Results of the Aortas.

No	ACC	Precision	Recall	F_1	JS	MCC
1	0.9858	0.7283	0.8298	0.7758	0.6337	0.7702
2	0.9827	0.7636	0.4544	0.5698	0.3984	0.5814
3	0.9901	0.6837	0.8062	0.7399	0.5872	0.7375
4	0.9888	0.8139	0.673	0.7368	0.5832	0.7345
Average	0.9869	0.7474	0.6909	0.7056	0.5506	0.7059

MOG2 (Zivkovic & Heijden, 2006), DenseUNet, OTSU (Otsu, 2007), K-means (Wang & Pan, 2014), and the watershed algorithm (Li et al., 2010), where ViBe, KNN, and MOG2 are motion-detection algorithms applied to the videos of blood flow, as shown in Figure 3a, and DenseUNet, OTSU, K-means, and the watershed algorithm are image segmentation algorithms applied to the visualized image of the average optical flow field, as shown in

Figure 3c. In this way, we analyzed the performance of the proposed method from both motion-detection and image segmentation perspectives.

Table 5 shows the quantitative results of the proposed method and the other algorithms on the zebrafish embryos. The accuracy of our work is much more superior than that of other algorithms. Meanwhile, the proposed method achieves the highest F_1 score

Table 3. Quantitative Classification Results of the Cardinal Veins.

No	ACC	Precision	Recall	F_1	JS	MCC
1	0.9789	0.7843	0.3264	0.461	0.2995	0.4979
2	0.983	0.9084	0.2253	0.361	0.2203	0.4477
3	0.9914	0.9046	0.5551	0.688	0.5244	0.705
4	0.9837	0.7966	0.2329	0.3604	0.2198	0.4255
Average	0.9843	0.8485	0.3349	0.4676	0.3160	0.5190

Table 4. Quantitative Classification Results of the Capillaries.

No	ACC	Precision	Recall	F_1	JS	MCC
1	0.9668	0.4064	0.4378	0.4215	0.267	0.4047
2	0.9652	0.2713	0.415	0.3281	0.1962	0.3185
3	0.9733	0.3337	0.4578	0.386	0.2392	0.3776
4	0.9736	0.2301	0.4139	0.2957	0.1735	0.2962
Average	0.9697	0.3104	0.4311	0.3578	0.2190	0.3493

and JS values. It performs the best in terms of the MCC as well. From both motion-detection and image segmentation perspectives, the proposed method maintains the highest AUC value of 0.9220, indicating that our method separates the two classes (vessel and nonvessel) significantly better than the existing approaches for all possible threshold values.

Figure 7 shows the visual segmentation results obtained via the abovementioned algorithms. Figures 7c–7f show the results of the image segmentation algorithms, including K-means, the watershed algorithm, DenseUNet, and OTSU. It is obvious that almost no capillaries are segmented, and the main vascular structure is badly discontinuous. Their failure to detect the whole vascular structure is attributed to the visualized image of the average optical flow field, which loses the key information of slow motion in vessels during velocity visualization. Figures 7h–7j show the results of the motion-detection algorithms, including MOG2, KNN, and ViBe. Although these methods can detect the rough shape of the vascular structure, the segmentation results only contain partial information of each vessel with much noise, poor continuity, and poor integrity. Our proposed method, as shown in Figure 7g, captures almost all vessels with high continuity and integrity. These qualitative results demonstrate the superiority of the proposed method, especially for narrow vessels, as shown in the red dashed circle. In addition, the proposed method reduces vessel breakages and background noise, outperforming the other methods in connectivity.

In summary, compared with the other seven algorithms, the proposed method achieves outstanding performance. The vessels in the segmented images produced by our method are more similar to the reference, indicating that our method is undoubtedly the state-of-the-art for transparent vessels.

Frame Temporal Resolution Analysis

The proposed method achieves outstanding performance using videos with 50 fps as input, of which the sampling interval is
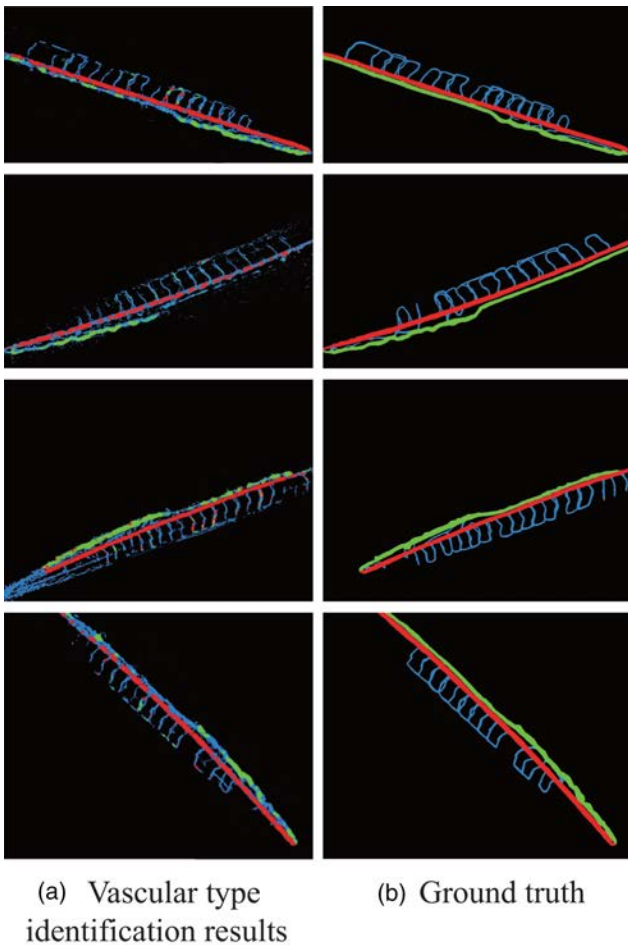
(a) Vascular type identification results

(b) Ground truth

Fig. 6. Global vascular-type identification results of four zebrafish embryos, where red and green vessels represent the aorta and cardinal vein, respectively, and blue vessels represent the capillaries.

Table 5. Quantitative Comparison With Related Algorithms on Zebrafish Embryos.

Algorithm	ACC	Precision	Recall	F_1	JS	MCC	AUC
DenseUNet	0.886	0.9832	0.5178	0.6784	0.5133	0.6639	0.7865
K-means	0.8245	0.9956	0.2452	0.3934	0.2449	0.4453	0.6636
OTSU	0.8098	0.9981	0.1808	0.3062	0.1808	0.3801	0.6262
Watershed	0.8241	0.9903	0.2447	0.3925	0.2441	0.443	0.6565
ViBe	0.828	0.9898	0.2618	0.414	0.2611	0.459	0.723
KNN	0.8939	0.9398	0.5799	0.7173	0.5592	0.6854	0.8389
MOG2	0.9007	0.8922	0.651	0.7527	0.6035	0.706	0.8553
Proposed	0.9798	0.8474	0.8308	0.8365	0.7217	0.8273	0.922
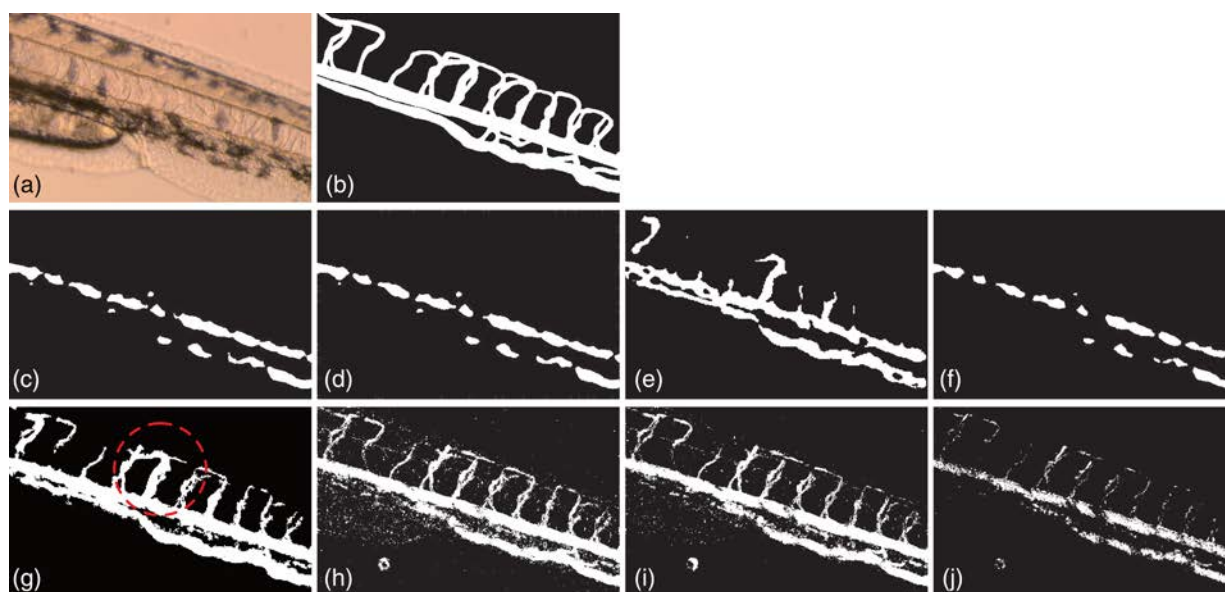
Fig. 7 - Colour online, Colour in print

Fig. 7. Segmentation results of (**a**) via application of (**c**) K-means, (**d**) the watershed algorithm, (**e**) DenseUNet, and (**f**) OTSU to the visualized image of the average optical flow field and application of (**g**) the proposed method, (**h**) MOG2, (**i**) KNN, and (**j**) ViBe to the raw video; (**b**) ground truth of (**a**).

20 ms. To investigate the effect of worsening frame temporal resolution of videos on the performance of our proposed method, we applied our method to downsampled videos with different sampling intervals ranging from 20 to 640 ms.

Figure 8 shows a plot of the quantitative segmentation results of the proposed method on videos with different temporal resolutions, where the x-axis denotes the linear value of the sampling intervals after applying the logarithmic function. When the sampling interval is extended to 320 ms, that is, the temporal resolution reduces to 3.125 fps, the proposed method maintains an accuracy of more than 90%. Moreover, the values of AUC, precision, and F_1 all decrease smoothly when the sampling interval of the input videos increases from 20 to 320 ms but decrease sharply when the sampling interval is extended to 640 ms.

Figure 9 shows the qualitative segmentation results obtained on videos with different temporal resolutions. Figures 9a–9k show that the performance does not obviously decrease, even when using videos with a 320 ms sampling interval, which is 16 times that of the original videos with 50 fps. Figure 9l indicates that the more severe loss of time resolution causes obvious vessel breakage and poor connectivity.
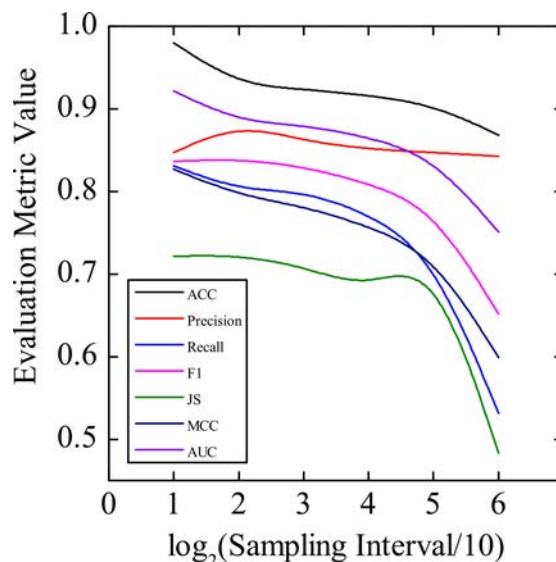

Fig. 8. Plot of the quantitative segmentation results of the proposed method on videos with different temporal resolutions.
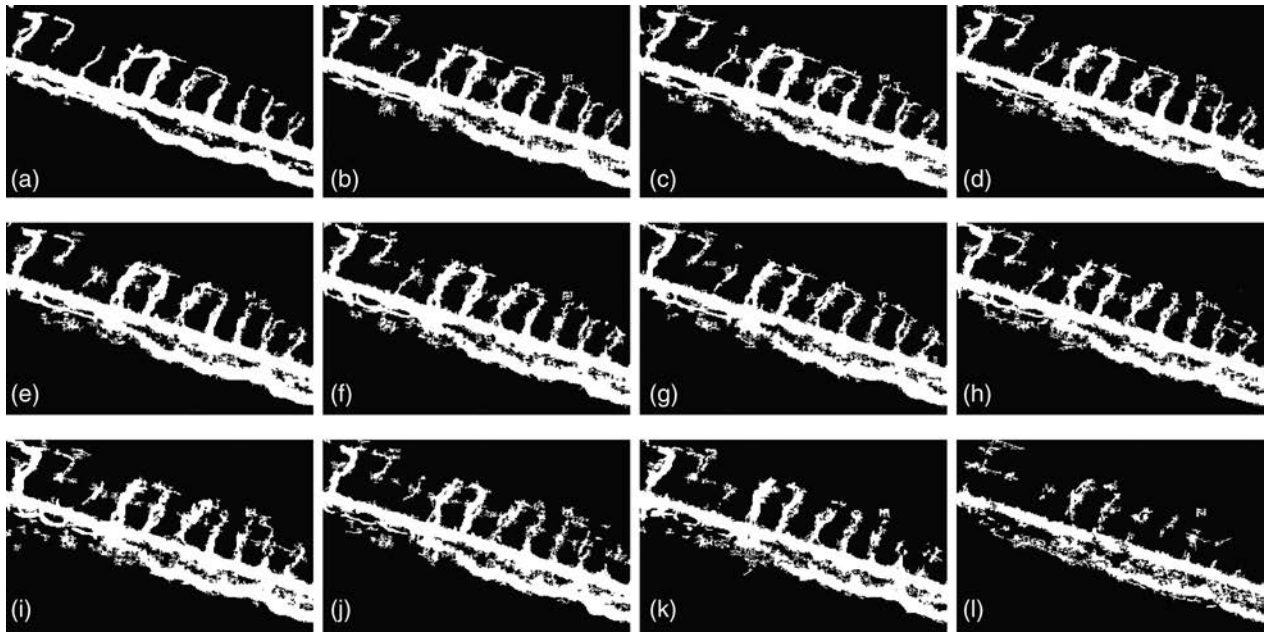
Fig. 9. Segmentation results of the proposed method on videos with different temporal resolutions. The sampling intervals are (**a**) 20 ms (50 fps), (**b**) 40 ms (25 fps), (**c**) 60 ms (16.6 fps), (**d**) 80 ms (12.5 fps), (**e**) 100 ms (10 fps), (**f**) 120 ms (8.3 fps), (**g**) 140 ms (7.14 fps), (**h**) 160 ms (6.25 fps), (**i**) 180 ms (5.5 fps), (**j**) 200 ms (5 fps), (**k**) 320 ms (3.125 fps), and (**l**) 640 ms (1.5625 fps).

In general, compared with the optimal videos with 50 fps, the loss in temporal resolution within a certain range only results in a slight decrease in accuracy and integrity and cannot worsen the success of the proposed method. The necessary minimal temporal resolution for successful segmentation is 3.125 fps, that is, the sampling interval of the video should not exceed 320 ms. This would enable us to speed up the process and reduce the computational cost and storage requirements, which is an advantage of micromanipulation systems.

Discussion

This study aims to achieve automated *in vivo* transparent vessel segmentation and identification for further subsequent research, for example, cardiovascular research (Li et al., 2019) and *in vivo* biological micromanipulations (Chan & Liebling, 2015; Menon et al., 2016; Sun et al., 2021). Our validations show that the proposed method identifies the vascular structure with high connectivity and integrity when applied to zebrafish embryos. The vascular types are identified with good accuracy, especially the main vessels, such as the aorta and cardinal vein of the zebrafish embryo. The proposed method was compared with other segmentation methods. The comparison results indicate the superiority of our method from both image segmentation and motion-detection perspectives. The experiments using downsampled videos indicate that a loss in temporal resolution within a certain range cannot worsen the success of the proposed method. The necessary minimal temporal resolution for successful segmentation is 3.125 fps.

The key to the success of the proposed method is the usage of the blood flow characteristics and motion features, especially the flow-connectivity features. We considered the motion of the RBCs and detected the vessel pixels based on the connectivity information. Meanwhile, the per-pixel machine learning classifier, that is, the random forest, had good adaptation, enhancing the robustness of our method for different scales of motion in vessels of different sizes.

However, one limitation of the proposed method is its sensitivity to motion in capillaries. The qualitative segmentation results show capillaries with less continuity and integrity than the ground truth. Because velocity normalization during optical flow field visualization easily leads to the loss in key slow motion information, especially in capillaries, the visualized image fails to express the full structure of related vessels. Hence, the image segmentation methods show less continuity in capillaries. Additionally, motion-detection algorithms tend to capture instantaneous motion. While it is obvious that there are no RBCs moving in the capillaries during the short videos captured, these motion-detection algorithms easily introduce noise, discontinuity and incompleteness in the segmentation results. These factors limit the ability of our method to segment complete capillary structures.

Notably, the partial absence of capillaries in the segmentation results is beyond the scope of image segmentation research. Considering the continuity of RBC movement, we will introduce the vascular connection path reasoning mechanism and combine RBC kinematics modeling and vascular tracking to obtain a more complete vascular structure in the future.

Conclusion

In this paper, we present a new machine learning method for automated *in vivo* transparent vessel segmentation and identification based on blood flow characteristics. Aiming at the fuzzy edges and the barely noticeable tubular characteristics of the vessels, we deal with the complex transparent vessel segmentation task by analyzing the motion of RBCs in vessels. The motion features of the RBCs are extracted and utilized to classify the vessel pixels. The characteristics of the blood flow also benefit the identification of different vascular types.

Taking zebrafish embryos as an example, we conducted quantitative and qualitative transparent vessel segmentation and identification experiments. The proposed method achieved a high accuracy of

97.98% in vessel segmentation, indicating the great similarity of the segmentation result and ground truth. The vascular types were identified with good accuracy of more than 96%, especially the aorta and cardinal vein. Compared with seven other algorithms, including segmentation algorithms and motion-detection algorithms, the proposed method achieved the highest accuracy, F_1, JS, MCC, and AUC values, demonstrating its outstanding performance. When the sampling interval was reduced from 20 to 320 ms, the proposed method maintained a high accuracy of more than 90%, demonstrating its good robustness on videos with worsening time resolutions.

However, in the segmentation image of the vascular structure, the capillaries were not completely continuous. This is mainly because the visualized image of the average optical flow field loses key slow motion information in vessels during velocity visualization or there are no RBCs moving in the capillaries during the short videos. In the future, we will combine the vascular tracking method to obtain a more complete vascular structure.

Conflict of interest. The authors declare that they have no known competing financial interests or personal relationships that could have appeared to influence the work reported in this paper.

References

Alhussein M, Aurangzeb K & Haider SI (2020). An unsupervised retinal vessel segmentation using Hessian and intensity based approach. *IEEE Access* **8**, 165056–165070.

Arcese L, Fruchard M & Ferreira A (2013). Adaptive controller and observer for a magnetic microrobot. *IEEE Trans Rob* **29**(4), 1060–1067.

Barnich O & Droogenbroeck MV (2011). ViBe: A universal background subtraction algorithm for video sequences. *IEEE Trans Image Process* **20**(6), 1709–1724.

Bartyzel K (2016). Adaptive Kuwahara filter. *Signal Image Video Process* **10**(4), 663–670.

Cai S, Tian Y, Lui H, Zeng H, Wu Y & Chen G (2020). Dense-UNet: A novel multiphoton in vivo cellular image segmentation model based on a convolutional neural network. *Quantit Imaging Med Surg* **10**(6), 1275–1285.

Chan KG & Liebling M (2015). Estimation of divergencefree 3D cardiac blood flow in a zebrafish larva using multi-view microscopy. In *IEEE International Symposium on Biomedical Imaging*. IEEE Press.

Cho TS, Freeman WT & Tsao H (2007). A reliable skin mole localization scheme. In *IEEE 11th International Conference on Computer Vision*, pp. 1–8.

Daien V, Carriere I, Kawasaki R, Cristol JP, Villain M, Fesler P, Ritchie K & Delcourt C (2013). Retinal vascular caliber is associated with cardiovascular biomarkers of oxidative stress and inflammation: The POLA study. *PLoS One* **8**(7), e71089.

Dong HY, Kwon D, Yun ID & Sang UL (2008). Fast multiscale vessel enhancement filtering. *Proc SPIE Int Soc Opt Eng* **6914**, 691423.

Farnebck G (2003). Two-frame motion estimation based on polynomial expansion. In *13th Scandinavian Conference on Image Analysis (SCIA 2003)*, Vol. 2749, pp. 363–370. Springer-Verlag.

Feng J, Cheng SH, Chan PK & Ip HHS (2005). Reconstruction and representation of caudal vasculature of zebrafish embryo from confocal scanning laser fluorescence microscopic images. *Comput Biol Med* **35**(10), 915–931.

Flusser J, Farokhi S, Hoschl C, Suk T, Zitová B & Pedone M (2016). Recognition of images degraded by Gaussian blur. *IEEE Trans Image Process* **25**(2), 790–806.

Francia GA, Pedraza C, Aceves M & Tovar-Arriaga S (2020). Optics: Ordering points to identify the clustering structure. *IEEE Access* **8**, 38493–38500.

Frangi RF, Niessen WJ, Vincken KL & Viergever MA (1998). Multiscale vessel enhancement filtering. In *International Conference on Medical Image Computing & Computer-assisted Intervention*, Vol. 1496.

Guan S, Khan A, Sikdar S & Chitnis PV (2020). Fully dense UNet for 2D sparse photoacoustic tomography artifact removal. *IEEE J Bio Health Inform* **24**(2), 568–576.

Ip H, Feng JJ & Cheng SH (2002). Automatic segmentation and tracking of vasculature from confocal scanning laser fluorescence microscope using multi-orientation dissections. In *IEEE International Symposium on Biomedical Imaging*, pp. 249–252. IEEE Press.

İlk HG, Jane O & İlk Ö (2011). The effect of Laplacian filter in adaptive unsharp masking for infrared image enhancement. *Infrared Phys Technol* **54**(5), 427–438.

Jodoin PM & Mignotte M (2005). Motion segmentation using a k-nearest-neighbor-based fusion procedure of spatial and temporal label cues. In *Image Analysis and Recognition, Second International Conference, ICIAR*, Vol. 3656, pp. 778–788. Springer.

Kim J, Um S & Min D (2018). Fast 2D complex Gabor filter with kernel decomposition. *IEEE Trans Image Process* **27**(4), 1713–1722.

Kugler E, Plant K, Chico T & Armitage PA (2019). Enhancement and segmentation workflow for the developing zebrafish vasculature. *J Imaging* **5**, 14.

Li D, Zhang G, Wu Z & Yi L (2010). An edge embedded marker-based watershed algorithm for high spatial resolution remote sensing image segmentation. *IEEE Trans Image Process* **19**(10), 2781–2787.

Li M, Liu X & Feng X (2019). Cardiovascular toxicity and anxiety-like behavior induced by deltamethrin in zebrafish (*Danio rerio*) larvae. *Chemosphere* **219**(Mar), 155–164.

Li R, Zeng T, Peng H & Ji S (2017). Deep learning segmentation of optical microscopy images improves 3-D neuron reconstruction. *IEEE Trans Med Imaging* **36**(7), 1533–1541.

Li X, Chen H, Qi X, Dou Q, Fu CW & Heng PA (2018). H-DenseUNet: Hybrid densely connected UNet for liver and tumor segmentation from CT volumes. *IEEE Trans Med Imaging* **37**(12), 2663–2674.

Lorenz C, Carlsen IC, Buzug TM, Fassnacht C & Weese J (1997). A multiscale line filter with automatic scale selection based on the Hessian matrix for medical image segmentation. In *Scale-Space Theory in Computer Vision*. Lect Notes Comput Sci, Vol. 1252(1), pp. 152–163.

Ma Y, Hao H, Xie J, Fu H, Zhang J, Yang J, Wang Z, Liu J, Zheng Y & Zhao Y (2021). ROSE: A retinal OCT-angiography vessel segmentation dataset and new model. *IEEE Trans Med Imaging* **40**(3), 928–939.

Menon PG, Rochon ER & Roman BL (2016). In-vivo cell tracking to quantify endothelial cell migration during zebrafish angiogenesis. *SPIE Medical Imaging*. International Society for Optics and Photonics.

Oszust M (2018). No-reference image quality assessment with local features and high-order derivatives. *J Vis Commun Image Represent* **56**(Oct), 15–26.

Otsu N (2007). A threshold selection method from gray-level histograms. *IEEE Trans Syst Man Cybern* **9**(1), 62–66.

Perona P & Malik J (1990). Scale space and edge detection using anisotropic diffusion. *IEEE Trans Pattern Anal Mach Intell* **12**(7), 629–639.

Phellan R, Lindner T, Helle M, Falcao AX & Forkert ND (2018). Automatic temporal segmentation of vessels of the brain using 4D ASL MRA images. *IEEE Trans Biomed Eng* **65**(7), 1486–1494.

Rajalaxmi S & Nirmala S (2014). Entropy-based straight kernel filter for echocardiography image denoising. *J Digit Imaging* **27**(5), 610–624.

Rodrigues EO, Conci A & Liatsis P (2020). Element: Multi-modal retinal vessel segmentation based on a coupled region growing and machine learning approach. *IEEE J Bio Health Inform* **24**(12), 3507–3519.

Schindelin J, Arganda-Carreras I, Frise E, Kaynig V, Longair M, Pietzsch T, Preibisch S, Rueden C, Saalfeld S, Schmid B, Tinevez JY, White DJ, Hartenstein V, Eliceiri K, Tomancak P & Cardona A (2012). Fiji: An open-source platform for biological-image analysis. *Nat Methods* **9**(7), 676–682.

Seidelmann SB, Claggett B, Bravo P, Gupta A, Farhad H, Di Carli M & Solomon S (2016). Retina vessel caliber in atherosclerotic cardiovascular event prediction: The atherosclerosis in communities study. *J Am Coll Cardiol* **67**(13), 1893.

Staal J, Abramoff MD, Niemeijer M, Viergever MA & Ginneken BV (2004). Ridge-based vessel segmentation in color images of the retina. *IEEE Trans Med Imaging* **23**(4), 501–509.

Sun M, Li L, Yao Y, Wang Y, Gong H, Gao Q, Chen D & Zhao X (2021). Robotic cardinal vein microinjection of zebrafish larvae based on 3D positioning. In *International Conference on Robotics and Automation*, pp. 1256–1262.

Vincent L (1994). Morphological area openings and closings for grey-scale images. *Shape in Picture* **126**, 197–208.

Wang C, Oda M, Hayashi Y, Yoshino Y & Mori K (2019). Tensor-cut: A tensor-based graph-cut blood vessel segmentation method and its application to renal artery segmentation. *Med Image Anal* **60**, 101623.

Wang L & Pan C (2014). Robust level set image segmentation via a local correntropy-based k-means clustering. *Pattern Recognit* **47**(5), 1917–1925.

Witten IH, Frank E & Hall MA (2011). *Data Mining: Practical Machine Learning Tools and Techniques*. Amsterdam: Morgan Kaufmann, Elsevier.

Xu R, Liu T, Ye X & Chen YW (2020). Boosting connectivity in retinal vessel segmentation via a recursive semantics-guided network. In *Medical Image Computing and Computer Assisted Intervention - MICCAI 2020 - 23rd International Conference,* Vol. 12265, pp. 786–795.

Xu Y, Mao Z, Liu C & Wang B (2018). Pulmonary vessel segmentation via stage-wise convolutional networks with orientation-based region growing optimization. *IEEE Access* **6**, 71296–71305.

Yaacoub C & Daou RAZ (2019). Fractional order sobel edge detector. In *Ninth International Conference on Image Processing Theory, Tools and Applications, IPTA 2019*, pp. 1–5. IEEE Press.

Yan Q, Wang B, Zhang W, Luo C & You Z (2020). An attention-guided deep neural network with multi-scale feature fusion for liver vessel segmentation. *IEEE J Bio Health Inform* **25**(7), 2629–2642.

Yang WJ & Xu JY (2017). Recognition of blood vessels in image of zebrafish embryo based on improved AdaBoost network. *Transducer and Microsystem Technologies* **36**(8), 141–144.

Yip RKH, Rimes JS, Capaldo BD, Vaillant F, Mouchemore KA, Pal B, Chen Y, Surgenor E, Murphy AJ, Anderson RL, Smyth GK, Lindeman GJ, Hawkins ED & Visvader JE (2021). Mammary tumour cells remodel the bone marrow vascular microenvironment to support metastasis. *Nat Commun* **12**, 6920.

Zhang K, Zhang H, Zhou H, Crookes D, Li L, Shao Y & Liu D (2019). Zebrafish embryo vessel segmentation using a novel dual ResUNet model. *Comput Intell Neurosci* **2019**, 1–14.

Zhao H, Li H & Cheng L (2019). Improving retinal vessel segmentation with joint local loss by matting. *Pattern Recognit* **98**, 107068.

Zivkovic Z & Heijden F (2006). Efficient adaptive density estimation per image pixel for the task of background subtraction. *Pattern Recognit Lett* **27**(7), 773–780.